

# Electrostatic Steering of Thermal Emission with Active Metasurface Control of Delocalized Modes

Joel Siegel,\* Margaret Fortman, and Victor Watson Brar†  
*Department of Physics, University of Wisconsin-Madison, Madison WI 53606 USA*

Shinho Kim‡ and Min Seok Jang§  
*School of Electrical Engineering, Korea Advanced Institute of Science and Technology, Daejeon 34141, Korea*  
(Dated: August 17, 2023)

**Abstract** We theoretically describe and experimentally demonstrate a graphene-integrated metasurface structure that enables electrically-tunable directional control of thermal emission. This device consists of a dielectric slab that acts as a Fabry-Perot (F-P) resonator supporting long-range delocalized modes bounded on one side by an electrostatically tunable metal-graphene metasurface. By varying the Fermi level of the graphene, the accumulated phase of the F-P mode is shifted, which changes the direction of absorption and emission at a fixed frequency. We directly measure the frequency- and angle-dependent emissivity of the thermal emission from a fabricated device heated to 250°. Our results show that electrostatic control allows the thermal emission at 6.61  $\mu\text{m}$  to be continuously steered over 16°, with a peak emissivity maintained above 0.9. We analyze the dynamic behavior of the thermal emission steerer theoretically using a Fano interference model, and use the model to design optimized thermal steerer structures.

Keywords: Metasurface, Thermal emission, Graphene, Plasmon

The mid infrared (MIR) is an important band for applications ranging from free-space laser communications[1] to chemical sensing [2, 3]. An optimal MIR source for these applications would be narrowband, and also offer high speed directional control, such that the beam can be rastered over a range of angles, or have a controllable focal point. Typically, such beam-steering is achieved by reflecting a beam using mechanical devices such as gimbal-mounted mirrors[4], optical phased arrays of antenna[5, 6], or liquid crystal-based devices[7]. While each of these techniques have their own set of advantages and disadvantages, one limitation common to them all is that they require an external source of light, such as a quantum cascade laser.

An alternative source of MIR light is one that can be found everywhere, thermal radiation. Any material at a non-zero temperature will emit radiation over a broad range of frequencies which, at moderate temperatures (0-700°C), is peaked in the MIR. Though thermal emission is typically viewed as incoherent, isotropic, and broadband, recent advances in nanoengineering have demonstrated that it is possible to engineer the emissivity of a structured material to create narrowband[8] directional[9] emissions that exhibits coherence. These include metasurfaces composed of non-interacting, localized resonator elements tuned to specific wavelengths, such as metallic nanoantennas[10] or semiconducting nanostructures that exhibit sharp quasi bound-state-int the continuum resonances[11, 12]. To achieve coherent directional emission, meanwhile, structures that

support long-range delocalized modes can be utilized. These include surface waves that are out-coupled via gratings[9, 13, 14], F-P cavities[15], photonic crystals[16–18], epsilon near zero modes[19] and delocalized modes formed by coupled resonators[20–22]. In all of these demonstrated devices, heating is all that is required to produce the desired light as the relevant optical modes are excited thermally, thus providing an elegant source of MIR radiation.

Imparting tunability into such devices - which could allow for dynamic beam control and frequency shifting - requires the integration of materials with variable optical properties. Materials with temperature-dependent phases and/or indices, such as GST[23–25], VO<sub>2</sub>[26–29], or Si[30] have been utilized to create metasurfaces that control the magnitude and phase of scattered light in reflection or transmission geometries, but such materials are unsuitable for thermal emission devices that operate at high, constant temperatures. Alternatively, materials with indices that depend on carrier density, including graphene, III-V quantum wells and indium tin oxide (ITO), can be utilized to bestow electrostatic tunability on metasurfaces, and devices that control phase, frequency, and intensity of reflected light have been demonstrated[31–36]. These materials are also chemically and phase stable at high temperatures, which has enabled them to be integrated within thermal-control metasurfaces to electrostatically tune the intensity and frequency of incandescent light in the mid-IR[37–39]. Unfortunately, such materials also introduce ohmic loss which can, in some geometries, suppresses formation of the long-range delocalized modes that are necessary for coherent, directional thermal emission. As such, dynamic angular tuning of thermal emission is an outstanding problem in the field of thermal metasurfaces.

\* J.S. and S. K. contributed equally to this work.

† vbrar@wisc.edu

‡ J.S. and S. K. are equally contributed to this work.

§ jang.minseok@kaist.ac.kr

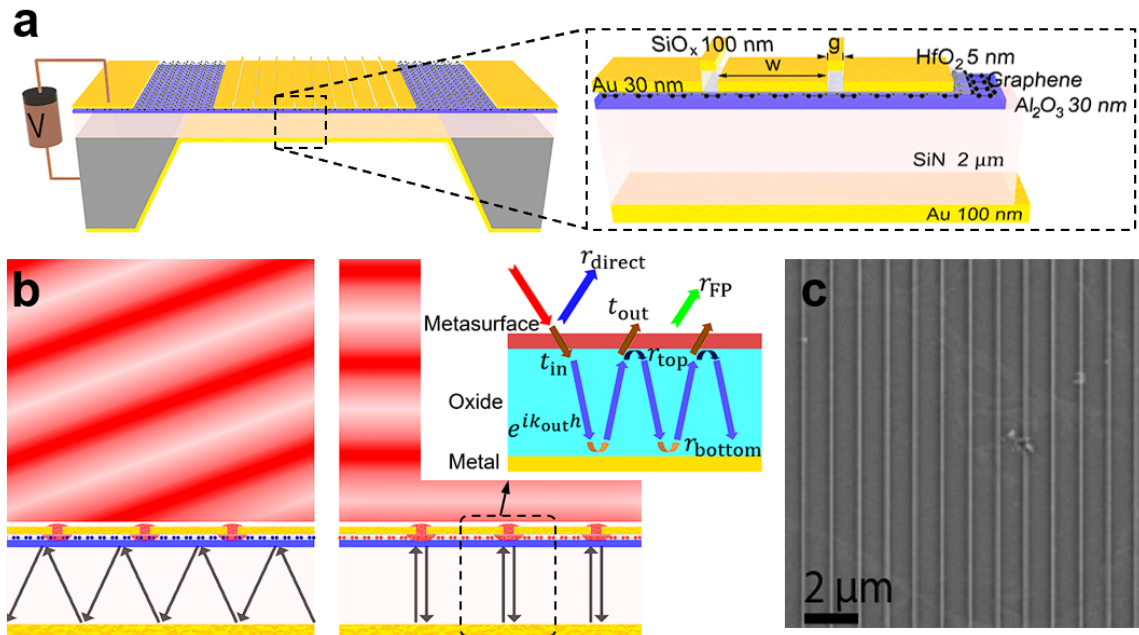


FIG. 1. The schematic of the fabricated thermal steering device. The zoomed view shows the geometry of a graphene-Au slit metasurface unit cell. (b) Schematic view of electrically tunable directional thermal emission by the graphene metasurface on the delocalized F-P photonic resonator. The emission angle of the structure is controlled by the Fermi level and incident angle-dependent resonant absorption condition. The inset shows decomposed total reflection into two reflection channels: direct reflection  $r_{\text{direct}}$  and F-P reflection  $r_{\text{FP}}$ . (c) scanning electron microscopy image of graphene metasurface on top of SiN<sub>x</sub> membrane. The width ( $w$ ) and gap ( $g$ ) of Au slit array are 1  $\mu\text{m}$  and 40 nm, respectively.

In this work, we theoretically describe and experimentally demonstrate a thermal emission device that can be tuned electrostatically to control the directionality of thermal emission within a narrow bandwidth. We show experimentally that by using a tunable graphene-integrated metasurface as a boundary for a delocalized F-P cavity mode, the thermal emission from a surface at  $6.61 \mu\text{m}$  ( $1508 \text{ cm}^{-1}$ ) can be continuously steered by  $\pm 16^\circ$  by changing the carrier density of the graphene sheet. Theoretical calculations, meanwhile, show that an optimized geometry using real materials could achieve  $\pm 60^\circ$  of continuous tuning.

For dynamic thermal emission steering, we utilize an electrically tunable F-P resonance of a SiN<sub>x</sub> dielectric layer sandwiched by a gold back reflector and a graphene-based active metasurface as illustrated in Fig. 1(a). The graphene metasurface consists of 30 nm thick, 1  $\mu\text{m}$  wide gold strips spaced 40 nm apart on top of HfO<sub>2</sub> (5 nm)/graphene/Al<sub>2</sub>O<sub>3</sub> (30 nm) trilayer, sitting on the 2  $\mu\text{m}$  thick SiN<sub>x</sub> membrane with the 100 nm gold back reflector that also serves as a back gate electrode. The gaps between the gold strips are filled with a bilayer of 30 nm gold and 100 nm SiO<sub>x</sub>. The sub-wavelength period of the structure suppresses far-field diffraction except for the zeroth order.

The working principle of our device is illustrated in Fig. 1(b). The graphene-based metasurface covering the top surface of the SiN<sub>x</sub> membrane acts as a partially reflecting mirror to form a vertical F-P cavity. By applying an electrostatic potential ( $V_G$ ) across the dielectric lay-

ers, the Fermi level of graphene ( $E_F$ ) is modulated and so are the complex reflection and transmission coefficients of the top graphene metasurface. Consequently, the condition for the resonance shifts, causing a shift in the peak emission angle ( $\theta$ ) for a given frequency. These changes can be qualitatively understood by treating the top metasurface as a two-dimensional sheet with an effective surface admittance, which is justified since the metasurface thickness is about two orders of magnitude shorter than the wavelength of the free space light[6, 31, 40]. In this model, the subwavelength metallic strips with narrow gaps make the overall optical response of the graphene metasurface to be highly capacitive (i.e. large imaginary impedance) at a low carrier concentration. As the conductivity of graphene raises with increasing  $E_F$ , the metasurface exhibits a reduced, but still high, capacitance and also acquires a larger conductance, changing the reflection/transmission characteristics. The quantitative surface admittance model for the graphene metasurface is discussed in detail in Supplementary Notes 1, 2, and 3.

Recognizing the emissivity  $\epsilon(\omega, \theta)$  of a reciprocal object is equal to its absorptivity  $\alpha(\omega, \theta)$ [41], one can understand the mechanism of the directional shift in thermal emission more intuitively by analyzing the absorption process. Since the transmission channel is blocked by the back reflector,

$$\epsilon = \alpha = 1 - |r_{\text{tot}}|^2 = 1 - |r_{\text{direct}} + r_{\text{FP}}|^2, \quad (1)$$

where  $r_{\text{tot}}$  is the total reflection, which can be decom-

posed into the direct reflection from the top surface ( $r_{\text{direct}}$ ) and the resonant reflection due to the F-P interference formed by multiple reflections inside the dielectric layer ( $r_{\text{FP}}$ ). The interplay between  $r_{\text{FP}}$  and  $r_{\text{direct}}$ , both of which are dependent on  $E_F$ , determines the overall absorption (and thus the emission) of the device. The absorption peak occurs when  $r_{\text{FP}}$  and  $r_{\text{direct}}$  destructively interfere with each other by having similar amplitudes and a  $\pi$  phase difference.

We first theoretically investigate the behavior of the proposed device using full-field electromagnetic simulations based on the finite element method as summarized in Fig. 2. The dependence of  $r_{\text{direct}}$  on  $\theta$  and  $E_F$  for TM polarized light is shown in Fig.2(c).  $r_{\text{direct}}$  can be obtained by simulating the reflection by the graphene metasurface sitting on a semi-infinite SiN<sub>x</sub> layer without a back reflector. Since the top graphene metasurface does not support any distinctive resonance around the target frequency of  $\omega = 1498 \text{ cm}^{-1}$ , the direct reflectance,  $R_{\text{direct}} = |r_{\text{direct}}|^2$ , exhibit a generic weak dependence on  $\theta$  within the range of  $0^\circ$  to  $50^\circ$ . As the carrier density of graphene increases, the metasurface becomes less capacitive, leading to better impedance matching as elaborated in (Supplementary Notes 1 and 3). Consequently,  $R_{\text{direct}}$  monotonically decreases with increasing  $E_F$ . The phase of the direct reflection,  $\phi_{\text{direct}} = \arg\{r_{\text{direct}}\}$ , remains nearly constant round  $0.9\pi$  within  $\theta \in (0^\circ, 50^\circ)$  and  $E_F \in (0.2, 0.65) \text{ eV}$ .

Unlike  $r_{\text{direct}}$ ,  $r_{\text{FP}}$  shows a strong dependence on both  $\theta$  and  $E_F$  due to its resonant nature. The F-P resonance occurs when the out-of-plane wavevector inside the dielectric,  $k_{\text{out}} = nk_0\sqrt{1 - \sin^2\theta}$ , satisfies the constructive interference condition:

$$2k_{\text{out}}h + \phi_{\text{top}} + \phi_{\text{bottom}} = 2\pi m, \quad (2)$$

where  $k_{\text{out}}h$  is the phase accumulation associated with vertical wave propagation across the dielectric layer,  $\phi_{\text{top}}$  and  $\phi_{\text{bottom}}$  are the reflection phase from the top and bottom surfaces, respectively, and  $m$  is an integer.  $\phi_{\text{bottom}} \sim \pi$  does not dependent on  $E_F$  since the bottom surface is a mere gold back reflector, which behaves like a perfect electric conductor at mid-infrared frequencies.  $\phi_{\text{top}}$ , in principle, could depend on  $E_F$  for metasurfaces with an admittance comparable to the surrounding medium, but in our device the admittance is large and, thus, the dependence of  $\phi_{\text{top}}$  is weak for  $E_F \in (0.2, 0.65) \text{ eV}$ . (see Supplementary Note 1 for a detailed analysis). As a result, at a fixed frequency, the resonance angle  $\theta_{\text{FP}}$  slightly decreases from  $34^\circ$  to  $28^\circ$  when  $E_F$  increases from  $0.2 \text{ eV}$  to  $0.65 \text{ eV}$  as indicated as a blue dashed curve in Fig.2(a); And, at a fixed  $\theta$ , the resonance frequency  $\omega_{\text{FP}}$  slightly blueshifts with increasing  $E_F$ . The F-P resonance becomes weaker with increasing  $E_F$  as the top graphene metasurface becomes less reflective and more absorptive, raising both the radiative and dissipative decay rate of the resonant mode. However, while  $\phi_{\text{top}}$  shows only a small dependence on  $E_F$ , the overall phase shift due to the F-P resonance ( $\phi_{\text{FP}}$ ) includes phase accumulated

while passing into and out of the F-P cavity, through the complex transmission coefficients  $t_{\text{in}}$  and  $t_{\text{out}}$ , which show considerably more dependence on  $E_F$ . (see Supplementary Note 3)

Since the amplitude of  $r_{\text{FP}}$  is similar to that of  $r_{\text{direct}}$  near the broad F-P resonance, what mainly determines the overall absorption is their phase difference,  $\phi_{\text{FP}} - \phi_{\text{direct}}$ . We note that the Fano interference between a non-resonant and a resonant scattering channel has been widely adopted to create a sharp resonant response[42, 43]. The dependence of  $\phi_{\text{FP}} - \phi_{\text{direct}}$  on  $E_F$  and  $\theta$ , which is dominated by  $\phi_{\text{FP}}$  due to the near constant  $\phi_{\text{direct}} \approx 0.9\pi$ , are plotted in Fig. 2(b).  $\phi_{\text{FP}}$  monotonically decreases with  $\theta$  because the propagation phase across the dielectric layer,  $k_{\text{out}}h$ , decreases as  $k_{\text{out}}$  shortens.  $\phi_{\text{FP}}$  also decreases with  $E_F$  as the capacitive phase shift of the top graphene metasurface reduces. As a result, the condition for the Fano resonance,  $\phi_{\text{FP}} - \phi_{\text{direct}} = \pi$ , shifts from  $\theta_{\text{res}} = 31^\circ$  to  $0^\circ$  as  $E_F$  alters from  $0.2 \text{ eV}$  to  $0.6 \text{ eV}$ . This change in the phase matching condition drives an overall change in the angular-dependent absorptivity/emissivity, shown in Fig.2(d), and thus allows the device to thermally emit at an angle that can be tuned by varying  $E_F$ .

In order to experimentally verify the possibility of active thermal emission steering, we fabricated the proposed device using e-beam lithography over a  $4 \times 4 \text{ mm}^2$  area (see Methods), heated it to  $250^\circ \text{C}$ , and measured its angle-dependent thermal emission spectra while varying the  $E_F$  by applying different gate voltages  $V_G$ . A polarizer was used to accept only TM polarized emission, and the acceptance angle of the emitted light was  $3^\circ$ . The emissivity of the structure is calculated by normalizing the emitted radiation of the device to the emitted radiation of a reference carbon nanotube blackbody[44].

The measured surface normal emissivity spectra for  $\theta = 0^\circ$  at  $V_G = 560, 0$  and  $-560 \text{ V}$ , shown in Fig.3(a), exhibit a well-defined resonance peak at around  $1.500 \text{ cm}^{-1}$  that blueshifts as the Fermi level of graphene increases, indicating that the thermal emission peaks are electrostatically tunable with minor variation in the intensity. The measured emissivity spectra also shows a strong angular dependence as shown in Fig.3(b). At a constant doping level ( $V_G = -560 \text{ V}$ ), the emission peak shifts from  $1508 \text{ cm}^{-1}$  to  $1543 \text{ cm}^{-1}$  as  $\theta$  changes from  $0^\circ$  to  $30^\circ$ . There are also higher order features present around  $2400 \text{ cm}^{-1}$  (see Supplementary Note 4) that show similar but more limited shifting. Finally, Fig.3(c) demonstrates the dynamic thermal emission steering by showing how the emission angle is modulated by altering the doping level of graphene at a fixed target frequency  $\omega = 1508 \text{ cm}^{-1}$ . At  $V_G = -560 \text{ V}$ , we observe that the emission peak is most intense at normal incidence and decreases in intensity as the angle is increased. As the applied gate voltage increases to  $560 \text{ V}$ , the lobe shifts from normal incidence to increasing angles, up to  $16^\circ$ , allowing for continuous tuning in that range.

These experimental results can be compared to simu-

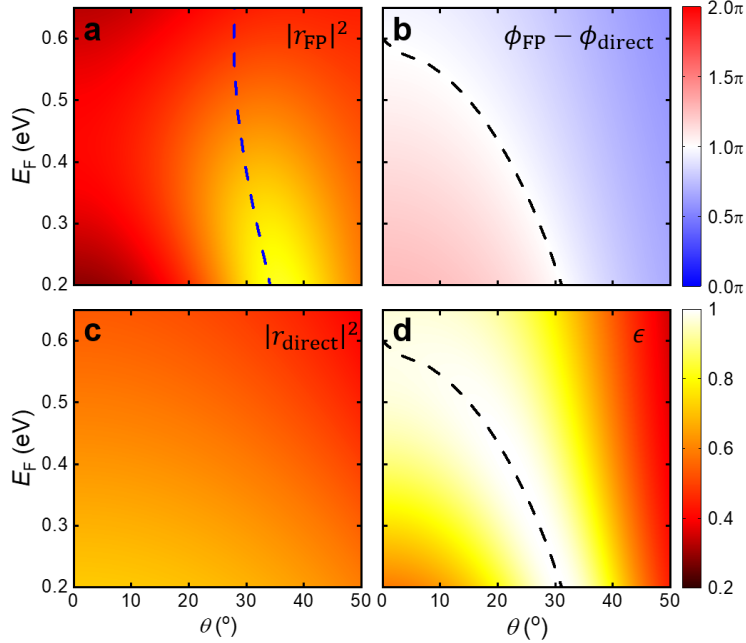


FIG. 2. Two distinct angular reflection spectra (a)  $|r_{\text{FP}}|^2$  and (c)  $|r_{\text{direct}}|^2$ . The blue dotted line indicates the F-P resonance condition. (b) The phase difference between two reflection coefficients ( $r_{\text{FP}} - r_{\text{direct}}$ ). (d) Calculated emissivity angular spectra. The black dotted line indicates the resonant absorption condition. The angular spectra are calculated for frequency  $\omega = 1498 \text{ cm}^{-1}$ .

lated emissivity spectra shown in Figures 3(d-f). In these simulations, the value of  $E_F$  at  $V_G = -560 \text{ V}$  was chosen as a fitting parameter and found to be  $-0.62 \text{ eV}$ , indicating that the sample is heavily hole-doped, which is consistent with previous studies of graphene grown and transferred using similar procedures[45]. Using this initial value of  $E_F$ , the Fermi energies at other gate voltages were derived with a simple capacitance model. The overall qualitative behavior of the simulations is consistent with our experimental finding, but the emission lobes are broader and the change of emission angle of the emitter is smaller in our experiment than was theoretically predicted. The likely sources of this inconsistency are the metastructure geometric and material parameter variations across the full  $4 \times 4 \text{ mm}^2$  device (see Subsections A and B in Supplementary Note 5), and carrier density variation during the heating process due to the temperature dependence of the  $\text{SiN}_x$ ,  $\text{Al}_2\text{O}_3$ , and  $\text{HfO}_2$  dielectric properties[46–51]. The estimated carrier density is also affected by substrate and interface charge traps, which can act to decrease the overall doping range (see Methods). We also note that the modulation depth at  $\theta \approx 0^\circ$  is predicted to be larger than what is observed experimentally, and we attribute this mostly to decreases in the magnitude of the graphene carrier density due to the filling of charge traps, as well as small potential misalignment of the heating stage. (see Methods) The intensity of emission at large angles can also be reduced due to ellipsoidal elongation of the measurement area which, for small device areas, can extend the active zone to include

some low emissivity, unpatterned gold areas.

To further explore the potential of the proposed thermal steerer device, we investigate the maximum realizable emission angle under the limitation of realistic geometric and material parameters. The Fermi level of graphene is assumed to be electrostatically tunable between  $0 \text{ eV}$  and  $0.6 \text{ eV}$ , considering typical dielectric strength of  $\text{SiN}_x$  and numerical optimizations of the geometric parameters of the device were performed to maximize the angle tunability. To prevent performance degradation due to non-local effects (see Supplementary Note 5 for more discussion), we set the minimum gap width to  $30 \text{ nm}$  and carried out simulations in the frame of classical electrodynamics. Figure 4(a) shows the structure of the optimized device. The gap and width of Au slit array are  $30 \text{ nm}$  and  $740 \text{ nm}$ , respectively. The  $\text{HfO}_2$  is thinned to  $1 \text{ nm}$  which is achievable smallest value that could avoid quantum tunneling effect. The bilayer Au/ $\text{SiO}_x$  area eliminated to enhance interaction between graphene and Au slit array. The optimization results show that it is possible to achieve  $\sim 60^\circ$  thermal emission angle steering with unity peak emissivity (Fig.4(b)). The achievable performance is greater than most metasurface-based electrically tunable beam steering devices[52] and is comparable to state-of-the-art MEMS-based beam steering device where field of view[53]. The improvements in the optimized structure in comparison to the experimentally measured sample are due to three main effects. First, the optimized structure utilized a smaller,  $30 \text{ nm}$  spacing between the gold strips. This acts to increase the elec-



## METHODS

### A. Fabrication of Device

2  $\mu\text{m}$  thick, 5 mm x 5 mm  $\text{SiN}_x$  membranes on a 200  $\mu\text{m}$  thick Si frame were purchased from Norcada. Metal deposition of the back-reflector consisted of a 2.5 nm chromium adhesion layer and 100 nm of gold. Atomic Layer Deposition (a Fiji G2 ALD) was used to grow a 30 nm film of  $\text{Al}_2\text{O}_3$  on the top of the  $\text{SiN}_x$  membrane. Once the  $\text{Al}_2\text{O}_3$  was grown, a prepared graphene sheet was transferred on top of the  $\text{Al}_2\text{O}_3$  film. Graphene was purchased from Grolltex and was grown on a Cu foil. To remove the foil, first a protective layer of PMMA (950k, A4, MicroChem Corp.) was added on top of the graphene. The Cu foil was etched away with  $\text{FeCl}_3$  (CE-100, Transene) then the graphene/PMMA stack was rinsed in a series of deionized water baths until transfer to the prepared membranes. Once transferred, the PMMA was removed by soaking in 60  $^\circ\text{C}$  acetone for 1 h. After the graphene transfer, a 5 nm film of  $\text{HfO}_2$  was grown via atomic layer deposition. To prepare the  $\text{SiN}_x$  membranes for the next steps, the Si frame of the sample was glued to a carrier Si chip with PMMA (950k, A8, MicroChem Corp.). The prepared substrate was then coated with a negative tone hydrogen silesquioxane resist (HSiQ, 6%, DisChem Inc.) at 100 nm. The sample was then exposed and patterned using the Elionix ELS G-100, an electron beam lithography tool. After exposure, the samples were developed in MF-321 for 90 s, with a 30 s rinse in DI water and then a 30 s rinse in IPA. The development process converts the exposed HSiQ to  $\text{SiO}_x$ . For metal deposition of the top, a metal mask was placed above the substrate to create electrically disconnected regions. The deposition consisted of a 2.5 nm chromium adhesion layer and 30 nm of gold. Following these processing steps, the graphene was found to be heavily hole-doped, similar to what has been observed in previous works[37, 45], Gate-dependent resistivity measurements showed an increase in resistance for positive gate bias, but no maximum resistance was observed that would indicate charge neutrality. These measurements also exhibited hysteresis, consistent with what has been observed elsewhere, and indicative of surface, interface, and substrate charge traps that can be populated with charge as  $V_G$  is changed. At high biases, these traps can screen the applied gating field without doping the graphene, leading to deviations from the simple capacitance model that we use to estimate the graphene carrier density for a given  $V_G$ [54–56].

### B. Thermal Emission Measurements

The emission measurements were performed using a Bruker Vertex 70 FTIR, where thermal emission from a heated sample was used as the lightsource of the interferometer. The device was mounted on a rotation stage, and thermal emission from the device is collected by the

aperture in the FTIR[44]. A carbon-nanotube source was used as our blackbody reference measurement. The finite size of the aperture creates a  $3^\circ$  acceptance angle, and there is also some uncertainty in the overall angle due to mechanical play in the stage holder and sample tilting within the sample holder. We estimate this uncertainly to be  $\leq 3^\circ$  based on measurements with an alignment laser reflected off of an unpatterned area of the sample surface.

### C. Optical Simulations

The frequency-dependent dielectric functions of  $\text{Al}_2\text{O}_3$ , Cr, Au and  $\text{SiO}_x$  were taken from the Palik data[57]. The dielectric functions of  $\text{HfO}_2$  and  $\text{SiN}_x$  were obtained from infrared ellipsometry[31]. Heat-induced dielectric function change of  $\text{SiN}_x$  is corrected through the higher-order F-P resonance peak which is insensitive to Fermi level modulation (see Supplementary Note 4). The graphene was modeled as a layer with zero thickness, and its optical conductivity was calculated by Kubo formula [58]. The carrier mobility of graphene is assumed to be  $300 \text{ cm}^2/\text{Vs}$  which is comparable to a previously reported value [31]. The reflection/transmission coefficients and absorption spectrum of the proposed structure were calculated by full-wave simulation with the finite element method.

## ACKNOWLEDGEMENTS

J.S. and V.W.B were supported by the Gordon and Betty Moore Foundation through a Moore Inventors Fellowship. M.F. was supported by Office of Naval Research award N00014-20-1-2356. This work was also supported by the National Research Foundation of Korea (NRF) grants funded by the Ministry of Science, ICT and Future Planning (NRF-2022R1A2C2092095, S.K. and M.S.J.) and by the Ministry of Education (NRF-2022R1I1A1A01065727, S.K.).

## AUTHOR CONTRIBUTIONS

These authors contributed equally: Joel Siegel, Shinho Kim.

## CONFLICT OF INTERESTS

The authors declare no conflicts of interests.

- [1] P. Corrigan, R. Martini, E. A. Whittaker, and C. Bethea, *Opt. Express* **17**, 4355 (2009).
- [2] J. Haas and B. Mizaikoff, *Annual Review of Analytical Chemistry* **9**, 45 (2016).
- [3] D. Rodrigo, O. Limaj, D. Janner, D. Etezadi, F. J. G. de Abajo, V. Pruneri, and H. Altug, *Science* **349**, 165 (2015).
- [4] B.-W. Yoo, M. Megens, T. Chan, T. Sun, W. Yang, C. J. Chang-Hasnain, D. A. Horsley, and M. C. Wu, *Opt. Express* **21**, 12238 (2013).
- [5] J. Sun, E. Timurdogan, A. Yaacobi, E. S. Hosseini, and M. R. Watts, *Nature* **493**, 195 (2013).
- [6] S. Han, S. Kim, S. Kim, T. Low, V. W. Brar, and M. S. Jang, *ACS Nano* **14**, 1166 (2020).
- [7] J. A. Frantz, J. D. Myers, R. Y. Bekele, C. M. Spillmann, J. Naciri, J. Kolacz, H. G. Gotjen, V. Q. Nguyen, C. C. McClain, L. B. Shaw, and J. S. Sanghera, *J. Opt. Soc. Am. B* **35**, C29 (2018).
- [8] Z. Wang, J. K. Clark, Y.-L. Ho, B. Vilquin, H. Daiguji, and J.-J. Delaunay, *ACS Photonics* **5**, 2446 (2018).
- [9] J.-J. Greffet, R. Carminati, K. Joulain, J.-P. Mulet, S. Mainguy, and Y. Chen, *Nature* **416**, 61–64 (2002).
- [10] X. Liu, T. Tyler, T. Starr, A. F. Starr, N. M. Jokerst, and W. J. Padilla, *Phys. Rev. Lett.* **107**, 045901 (2011).
- [11] C. F. Doiron and G. V. Naik, *Advanced Materials* **31**, 1904154 (2019).
- [12] K. Sun, Z. Zhao, Y. Cai, U. Levy, and Z. Han, *Nanophotonics* **10**, 4035 (2021).
- [13] M.-W. Tsai, T.-H. Chuang, C.-Y. Meng, Y.-T. Chang, and S.-C. Lee, *Applied physics letters* **89** (2006).
- [14] A. Ghanekar, R. Kapadia, and M. L. Povinelli, *Journal of Quantitative Spectroscopy and Radiative Transfer* **293**, 108367 (2022).
- [15] L. Wang, B. Lee, X. Wang, and Z. Zhang, *International Journal of Heat and Mass Transfer* **52**, 3024 (2009).
- [16] B. Lee, C. Fu, and Z. Zhang, *Applied Physics Letters* **87** (2005).
- [17] I. Celanovic, D. Perreault, and J. Kassakian, *Physical Review B* **72**, 075127 (2005).
- [18] A. Battula and S. Chen, *Physical Review B* **74**, 245407 (2006).
- [19] J. Xu, J. Mandal, and A. P. Raman, *Science* **372**, 393 (2021).
- [20] A. C. Overvig, S. A. Mann, and A. Alù, *Physical Review X* **11**, 021050 (2021).
- [21] A. Weiss, C. Frydendahl, J. Bar-David, R. Zektzer, E. Edrei, J. Engelberg, N. Mazurski, B. Desiatov, and U. Levy, *ACS Photonics* **9**, 605 (2022).
- [22] J. R. Nolen, A. C. Overvig, M. Cotrufo, and A. Alù, *arXiv preprint arXiv:2301.12301* (2023).
- [23] C. H. Chu, M. L. Tseng, J. Chen, P. C. Wu, Y.-H. Chen, H.-C. Wang, T.-Y. Chen, W. T. Hsieh, H. J. Wu, G. Sun, *et al.*, *Laser & Photonics Reviews* **10**, 986 (2016).
- [24] S. Abdollahramezani, O. Hemmatyar, M. Taghinejad, H. Taghinejad, A. Krasnok, A. A. Eftekhar, C. Teichrib, S. Deshmukh, M. A. El-Sayed, E. Pop, *et al.*, *Nature communications* **13**, 1696 (2022).
- [25] Y. Zhang, C. Fowler, J. Liang, B. Azhar, M. Y. Shalaginov, S. Deckoff-Jones, S. An, J. B. Chou, C. M. Roberts, and V. Liberman, *Nature Nanotechnology* **16**, 661 (2021).
- [26] J. Rensberg, S. Zhang, Y. Zhou, A. S. McLeod, C. Schwarz, M. Goldflam, M. Liu, J. Kerbusch, R. Nawrodt, S. Ramanathan, *et al.*, *Nano letters* **16**, 1050 (2016).
- [27] M. T. Nouman, J. H. Hwang, M. Faiyaz, K.-J. Lee, D.-Y. Noh, and J.-H. Jang, *Optics express* **26**, 12922 (2018).
- [28] Y. Kim, P. C. Wu, R. Sokhoyan, K. Mauser, R. Glaudell, G. Kafaie Shirmanesh, and H. A. Atwater, *Nano letters* **19**, 3961 (2019).
- [29] R. Audhkhshi and M. L. Povinelli, *Optics Letters* **46**, 1768 (2021).
- [30] J. Sun, E. Timurdogan, A. Yaacobi, E. S. Hosseini, and M. R. Watts, *Nature* **493**, 195 (2013).
- [31] S. Kim, M. S. Jang, V. W. Brar, K. W. Mauser, L. Kim, and H. A. Atwater, *Nano Letters* **18**, 971 (2018).
- [32] J. Y. Kim, J. Park, G. R. Holdman, J. T. Heiden, S. Kim, V. W. Brar, and M. S. Jang, *Nature Communications* **13**, 2103 (2022).
- [33] S. Kim, S. G. Menabde, V. W. Brar, and M. S. Jang, *Advanced Optical Materials* **8**, 1901194 (2020).
- [34] Y.-W. Huang, H. W. H. Lee, R. Sokhoyan, R. A. Pala, K. Thyagarajan, S. Han, D. P. Tsai, and H. A. Atwater, *Nano letters* **16**, 5319 (2016).
- [35] R. Sarma, S. Campione, M. Goldflam, J. Shank, J. Noh, L. T. Le, M. D. Lange, P. D. Ye, J. Wendt, and I. Ruiz, *Applied Physics Letters* **113** (2018).
- [36] P. C. Wu, R. A. Pala, G. Kafaie Shirmanesh, W.-H. Cheng, R. Sokhoyan, M. Grajower, M. Z. Alam, D. Lee, and H. A. Atwater, *Nature communications* **10**, 3654 (2019).
- [37] V. W. Brar, M. C. Sherrott, M. S. Jang, S. Kim, L. Kim, M. Choi, L. A. Sweatlock, and H. A. Atwater, *Nat. Commun.* **6**, 7032 (2015).
- [38] J. Park, J.-H. Kang, X. Liu, S. J. Maddox, K. Tang, P. C. McIntyre, S. R. Bank, and M. L. Brongersma, *Science Advances* **4**, eaat3163 (2018).
- [39] T. Inoue, M. D. Zoysa, T. Asano, and S. Noda, *Nat. Mater.* **13**, 928 (2014).
- [40] M. S. Jang, V. W. Brar, M. C. Sherrott, J. J. Lopez, L. Kim, S. Kim, M. Choi, and H. A. Atwater, *Phys. Rev. B* **90**, 165409 (2014).
- [41] G. Kirchhoff, *Annalen der Physik* **185**, 275 (1860).
- [42] A. E. Miroshnichenko, S. Flach, and Y. S. Kivshar, *Rev. Mod. Phys.* **82**, 2257 (2010).
- [43] M. S. Jang, S. Kim, V. W. Brar, S. G. Menabde, and H. A. Atwater, *Phys. Rev. Appl.* **10**, 054053 (2018).
- [44] Y. Xiao, A. Shahsafi, C. Wan, P. J. Roney, G. Joe, Z. Yu, J. Salman, and M. A. Kats, *Phys. Rev. Appl.* **11**, 014026 (2019).
- [45] J. F. Siegel, J. H. Dwyer, A. Suresh, N. S. Safron, M. A. Fortman, C. Wan, J. W. Choi, W. Wei, V. Saraswat, W. Behn, M. A. Kats, M. S. Arnold, P. Gopalan, and V. W. Brar, *ACS Photonics* **8**, 1277 (2021).
- [46] K.-H. Allers, *Microelectronics Reliability* **44**, 411 (2004).
- [47] A. Bellucci, G. Sabbatella, M. Girolami, M. Mastellone, V. Serpente, A. Mezzi, S. Kaciulis, B. Paci, A. Generosi, R. Polini, *et al.*, *Energy Technology* **9**, 2000788 (2021).
- [48] M. Bülbül, *Microelectronic engineering* **84**, 124 (2007).
- [49] L.-Y. Chen and G. W. Hunter, *MRS Online Proceedings Library (OPL)* **833**, G7 (2004).

- [50] H. S. Dow, W. S. Kim, and J. W. Lee, *AIP Advances* **7** (2017).
- [51] W. Zhu, T.-P. Ma, T. Tamagawa, J. Kim, and Y. Di, *IEEE Electron Device Letters* **23**, 97 (2002).
- [52] P. Berini, *ACS Photonics* **9**, 2204 (2022).
- [53] X. Zhang, K. Kwon, J. Henriksson, J. Luo, and M. C. Wu, *Nature* **603**, 253 (2022).
- [54] M. Bonmann, *Effects of impurities on charge transport in graphene field-effect transistors* (Chalmers Tekniska Hogskola (Sweden), 2017).
- [55] Y.-X. Lu, C.-T. Lin, M.-H. Tsai, and K.-C. Lin, *Micro-machines* **13**, 509 (2022).
- [56] M. Bartosik, J. Mach, J. Piastek, D. Nezval, M. Konecny, V. Svarc, K. Ensslin, and T. Šikola, *ACS sensors* **5**, 2940 (2020).
- [57] E. D. PALIK, *Handbook of Optical Constants of Solids*, edited by E. D. PALIK (Academic Press, Boston, 1998).
- [58] L. A. Falkovsky, *Journal of Physics: Conference Series* **129**, 012004 (2008).